Combination of fast-ion diagnostics in velocity-space tomographies

2013 Nucl. Fusion 53 063019

(http://iopscience.iop.org/0029-5515/53/6/063019)

IOP Publishing and International Atomic Energy Agency Nuclear Fusion

Nucl. Fusion **53** (2013) 063019 (10pp) doi:10.1088/0029-5515/53/6/063019

Combination of fast-ion diagnostics in velocity-space tomographies

M. Salewski[1], B. Geiger[2], S.K. Nielsen[1], H. Bindslev[3], M. García-Muñoz[2], W.W. Heidbrink[4], S.B. Korsholm[1], F. Leipold[1], J. Madsen[1], F. Meo[1], P.K. Michelsen[1], D. Moseev[2,5], M. Stejner[1], G. Tardini[2] and the ASDEX Upgrade Team[2]

[1] Association Euratom-DTU, Technical University of Denmark, Department of Physics, DTU Risø Campus, DK-4000 Roskilde, Denmark
[2] Association Euratom-Max-Planck-Institut für Plasmaphysik, D-85748 Garching, Germany
[3] Aarhus University, Faculty of Science and Technology, DK-8000 Aarhus C, Denmark
[4] University of California, Irvine, Department of Physics and Astronomy, CA 92697, USA
[5] Association Euratom-FOM Institute DIFFER, 3430 BE Nieuwegein, The Netherlands

E-mail: msal@fysik.dtu.dk

Received 22 October 2012, accepted for publication 17 April 2013
Published 14 May 2013
Online at stacks.iop.org/NF/53/063019

Abstract
Fast-ion D_α (FIDA) and collective Thomson scattering (CTS) diagnostics provide indirect measurements of fast-ion velocity distribution functions in magnetically confined plasmas. Here we present the first prescription for velocity-space tomographic inversion of CTS and FIDA measurements that can use CTS and FIDA measurements together and that takes uncertainties in such measurements into account. Our prescription is general and could be applied to other diagnostics. We demonstrate tomographic reconstructions of an ASDEX Upgrade beam ion velocity distribution function. First, we compute synthetic measurements from two CTS views and two FIDA views using a TRANSP/NUBEAM simulation, and then we compute joint tomographic inversions in velocity-space from these. The overall shape of the 2D velocity distribution function and the location of the maxima at full and half beam injection energy are well reproduced in velocity-space tomographic inversions, if the noise level in the measurements is below 10%. Our results suggest that 2D fast-ion velocity distribution functions can be directly inferred from fast-ion measurements and their uncertainties, even if the measurements are taken with different diagnostic methods.

(Some figures may appear in colour only in the online journal)

1. Introduction

ASDEX Upgrade is a medium-size tokamak that is equipped with powerful and versatile auxiliary heating systems: a variety of fast-ion populations can be generated by eight neutral beam injection (NBI) sources with a total power of 20 MW and four ion cyclotron resonance heating (ICRH) antennas with a total power of 6 MW [1–3]. ASDEX Upgrade is also equipped with a suite of fast-ion diagnostics: fast-ion loss detectors (FILDs) [4–6], fast-ion D_α (FIDA) [7], collective Thomson scattering (CTS) [8–13], neutron spectrometry [14, 15], neutral particle analysers (NPA) [16, 17] and γ-ray spectrometry [18]. These auxiliary heating systems and fast-ion diagnostics give unique opportunities to study fast ions in tokamak plasmas. Each diagnostic observes fast ions in different, restricted parts of configuration space and velocity space. CTS and FIDA diagnose confined fast ions in small volumes relative to the plasma size. FILDs are sensitive to lost fast ions near the plasma edge that strike the scintilator plates. Passive NPAs, neutron spectrometers and γ-ray spectrometers detect confined fast ions anywhere along the lines-of-sight.

We focus here on CTS and FIDA measurements that could be made at roughly the same location in configuration space. CTS and FIDA measure spectra of scattered and emitted radiation, respectively, that constitute 1D functions of the fast-ion velocity distribution function. Traditionally, fast-ion CTS or FIDA measurements are often compared with simulated spectra to investigate if the measurements match the expectation or if they are anomalous [9, 19, 20]. Orbit-following codes such as TRANSP/NUBEAM provide the local 2D fast-ion velocity distribution function f, and then synthetic measurements are calculated from f. However, if the real measurements disagree with the synthetic measurements, it is often unclear what caused this discrepancy. Our final goal is to experimentally determine f, and this might help establish where in 2D velocity space the measurements

disagree with the simulation. Inference of tomographic inversions in velocity space from CTS or FIDA measurements was recently shown to be an achievable goal [13]. Velocity-space tomographic inversions are the best fit to the CTS and FIDA measurements under a regularization condition. It was also shown that the resemblance of the inversions with the original 2D ion velocity distribution function improves with the number of available views, and this motivates the combination of CTS and FIDA measurements in joint velocity-space tomographic inversions. Here we derive a new prescription for velocity-space tomography that allows such a combination of diagnostics which was not possible with previous methods [13]. Our new prescription is also the first to account for uncertainty in the individual measurements. Lastly, we here present a method to estimate uncertainty levels in the tomographic inversions.

Among the most wide-spread applications of computed tomography in configuration space are medical imaging, e.g. x-ray computed axial tomography (CAT or CT) scanners, positron emission tomography (PET) scanners or magnetic resonance imaging (MRI) scanners [21, 22], and it is also widely used in nuclear fusion research [23–32]. Velocity-space tomography is less developed [13, 33, 34] but could be particularly useful in studies of selective ejection or redistribution in velocity space. Several types of modes affect ions in only part of velocity space, for example sawteeth [35–38], Alfvén eigenmodes [6, 39–43] and neoclassical tearing modes [4, 5]. Turbulent transport of fast ions also depends on the ion energy [44–47]. Additionally, velocity-space tomography could be used to monitor phase-space engineering of fast-ion velocity distribution functions which has enabled control of sawteeth and neoclassical tearing modes [48].

We compute joint tomographic inversions of 2D fast-ion velocity distribution functions from synthetic 1D CTS and FIDA measurements. The use of synthetic diagnostics gives us the advantage that we can compare the underlying, known 2D velocity distribution functions with the inversions. The synthetic measurements were calculated from a TRANSP/NUBEAM simulation for the combined four-view FIDA/CTS system at ASDEX Upgrade. Our joint tomography method could also combine the fast-ion charge exchange spectroscopy (FICXS) (that detects light other than D_α but is otherwise similar to FIDA) and the CTS diagnostics at the Large Helical Device (LHD) [49, 50]. Moreover, joint tomographic inversions could be directly relevant to ITER where the proposed FICXS [51] and the CTS system [52–55] could be combined even if there is only one CTS view. Measurements from any other fast-ion diagnostic could be included in our joint tomography prescription, if quantitative weight functions describing the measurements such as those for CTS [34] or FIDA [20, 56] can be formulated. Our joint tomography method would then also be applicable to other tokamaks with many-view FIDA systems and additional fast-ion diagnostics, for example DIII-D [57, 58], NSTX [59] and MAST. Here we make a start by combining CTS and FIDA.

In section 2 we describe the four-view CTS and FIDA system at ASDEX Upgrade, and in section 3 we discuss the combination of CTS and FIDA measurements and their uncertainties in a joint tomography prescription. Joint tomographic inversions of a simulated beam ion distribution function from combined synthetic CTS and FIDA measurements and their uncertainties are presented in section 4, and in section 5 we study the effect of noise. Finally, we discuss the intrinsically complementary nature of CTS and FIDA measurements in section 6, and we draw conclusions in section 7.

2. CTS and FIDA measurements at ASDEX Upgrade

The CTS system at ASDEX Upgrade has two receivers after installations in 2012, and likewise the FIDA system has two optical heads. CTS and FIDA measurements are sensitive to the velocity-space distribution in small measurement volumes. Except for different shapes and sizes of the measurement volumes, which we ignore here assuming measurements in spatial points, the CTS and FIDA measurements could be made at the same position assuming toroidal symmetry. Hence, four simultaneous views of the 2D fast-ion distribution function are now available if the CTS views and the FIDA views are used together. The spatial resolution of the CTS diagnostic at ASDEX Upgrade is about 10 cm which is given by the size of the intersection pattern of the probe beam from a gyrotron and the receiver field of view. The measurement positions can be moved freely in the plasma core by means of steerable antennas. The measurement locations of the two CTS views can be similar in the poloidal (R, Z) plane if two probe beams are used. The time resolution is often set to 4 ms given by the gyrotron modulation frequency. The position of a FIDA measurement is determined by the intersection of the NBI S3 beam path and the line-of-sight (LOS) of the optical head. The spatial resolution of the FIDA diagnostic at ASDEX Upgrade is about 7 cm, and the time resolution is 2 ms.

CTS and FIDA measure 1D functions g which depend on the respective projection angles ϕ_{CTS} and ϕ_{FIDA} and the fast-ion 2D velocity-space distribution function f that we assume to be rotationally symmetric about the magnetic field direction. CTS and FIDA weight functions relate the 2D fast-ion velocity distribution function f to the 1D measurements g [34, 56]. CTS and FIDA weight functions w are defined by

$$g_{\mathrm{CTS}}(u, \phi_{\mathrm{CTS}}) = \int_{-\infty}^{\infty}\int_{0}^{\infty} w_{\mathrm{CTS}}(u, \phi_{\mathrm{CTS}}, v_\parallel, v_\perp) f(v_\parallel, v_\perp) \mathrm{d}v_\perp \mathrm{d}v_\parallel, \quad (1)$$

$$g_{\mathrm{FIDA}}(\lambda, \phi_{\mathrm{FIDA}}) = \int_{-\infty}^{\infty}\int_{0}^{\infty} w_{\mathrm{FIDA}}(\lambda, \phi_{\mathrm{FIDA}}, v_\parallel, v_\perp) f(v_\parallel, v_\perp) \mathrm{d}v_\perp \mathrm{d}v_\parallel \quad (2)$$

where u is the projected velocity and λ is the wavelength of detected FIDA light. Examples of weight functions for CTS and FIDA for $\phi_{\mathrm{CTS}} = \phi_{\mathrm{FIDA}} = 64^\circ$ are shown in figure 1.

CTS diagnostics are sensitive to 1D projections of f onto the wave vector $\boldsymbol{k}^\delta = \boldsymbol{k}^s - \boldsymbol{k}^i$ which is the difference between the wave vectors of scattered radiation $\boldsymbol{k}^s$ and incident radiation $\boldsymbol{k}^i$. The most important angle to describe the pre-selected projection direction given by $\boldsymbol{k}^\delta$ is the projection angle $\phi_{\mathrm{CTS}} = \angle(\boldsymbol{k}^\delta, \boldsymbol{B})$ where $\boldsymbol{B}$ is the magnetic field. A frequency shift ν^δ of scattered radiation can be related to the ion velocity $\boldsymbol{v}$ projected onto $\boldsymbol{k}^\delta$:

$$\nu^\delta = \nu^\mathrm{s} - \nu^\mathrm{i} \approx \boldsymbol{v} \cdot \boldsymbol{k}^\delta / 2\pi = u k^\delta / 2\pi, \quad (3)$$

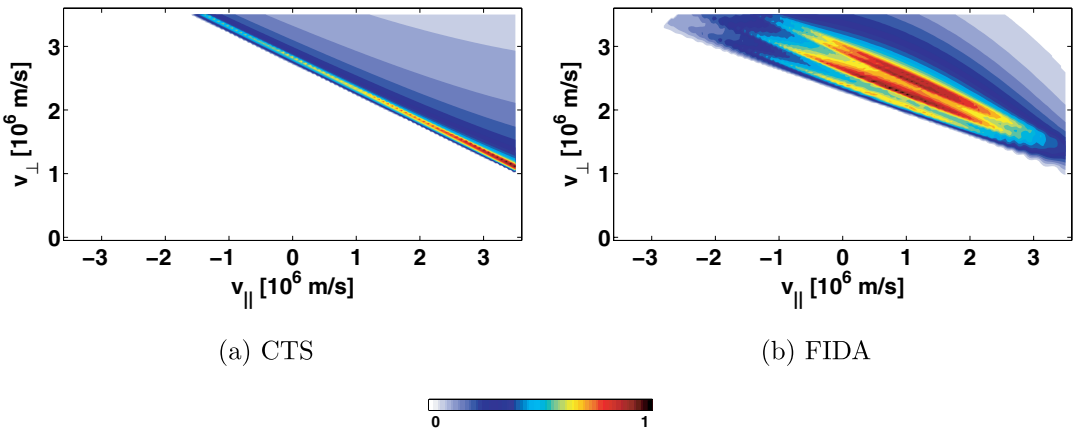

(a) CTS (b) FIDA

Figure 1. Weight functions [a.u.] at a projection angle of $\phi_{\mathrm{CTS}} = \phi_{\mathrm{FIDA}} = 64^\circ$ for (*a*) CTS and (*b*) FIDA and a particular velocity or wavelength interval.

where $k^\delta = |\boldsymbol{k}^\delta|$. We define here a CTS *measurement* as detection of the fast-ion phase-space density in a particular interval in u that is related to an interval in v^δ via equation (3). The projection angles ϕ_{CTS} of the two CTS views can be varied independently if two probe beams are used.

For FIDA, the fast ions likewise leave a spectral signature in the detected light by Doppler shift and Stark splitting. FIDA weight functions are directly parametrized by the wavelength of detected radiation λ instead of u [20, 56]. Hence we define here as FIDA *measurement* the detection of Doppler- and Stark-shifted light in a particular wavelength interval. The FIDA optical head observes NBI source S3 in the plasma core at two different fixed angles $\phi_{\mathrm{FIDA}} = \angle(\boldsymbol{k}^{\mathrm{LOS}}, \boldsymbol{B})$ where $\boldsymbol{k}^{\mathrm{LOS}}$ is the wave vector along the LOS of the optical heads. The toroidal LOS has an angle of $\phi_{\mathrm{FIDA}} = 11^\circ$, and the poloidal LOS, that was installed in 2012, has $\phi_{\mathrm{FIDA}} = 64^\circ$. The angles ϕ_{CTS} and ϕ_{FIDA} describing the *view*, the measurements g_{CTS} and g_{FIDA}, and the weight functions w_{CTS} and w_{FIDA} are analogous and will hereafter simply be called ϕ, g and w, respectively. The analogy between CTS and FIDA measurements is reflected in the form of the weight functions that can be chosen to be quite similar as we show in figure 1. We will discuss the differences between the CTS and FIDA weight functions with identical projection angle ϕ in section 6.

3. Prescription for joint tomographic reconstruction from measurements and their uncertainties

We discretize f and the measurements g from CTS and FIDA into f_{kl} and g_{ij} and the coordinates $(u, \phi, v_\parallel, v_\perp)$ into $(u_i, \phi_j, v_{\parallel k}, v_{\perp l})$. The discrete functions f_{kl} and g_{ij} are written into the column matrices F and G, respectively, similarly to the procedure in [13]. F is a column matrix of size $N \times 1$ obtained from the discrete 2D fast-ion velocity distribution function described by $N = K \times L$ grid points (K grid points in $v_\perp$ and L in $v_\parallel$). G is a column matrix of size $M \times 1$ consisting of the discrete 1D functions measured with CTS or FIDA. M is the total number of measurements in u_i (CTS) and λ_i (FIDA) made in the J views with projection angles ϕ_j. The subscripts i, j, k, l, m, n run from 1 to the corresponding upper case letter I, J, K, L, M, N. The discretized form of equations (1) and (2) is

$$g_{ij} = \sum_{k=1}^{K} \sum_{l=1}^{L} w_{ijkl} f_{kl} \Delta v_\perp \Delta v_\parallel, \tag{4}$$

where $\Delta v_\perp$ and $\Delta v_\parallel$ are the cell sizes in $v_\perp$ and $v_\parallel$, respectively. Using these discrete weight functions, we can immediately write down an $M \times N$ transfer matrix W taking F into G [13], and we obtain the linear system of equations

$$W F = G. \tag{5}$$

In real experiments the transfer matrix W and the measurements G are known, and tomographies can be found by solving the inverse problem in equation (5). If the measurements G contain noise, there is no exact solution irrespective of whether the system of equations is underdetermined or overdetermined, but we can find a best fit F^+ by minimizing a figure of merit χ^2. Whereas in [13] we assumed identical uncertainties in all measurements, we here allow for individual uncertainties $\sigma_{G,m}$ in each measurement. For correlated uncertainties in the measurements, the χ^2 figure of merit is determined by the covariance matrix of the measurements C_G and the misfit of the measurements [60]:

$$\chi^2 = \sum_{m,m'} \left(G_m - \sum_n W_{mn} F_n \right) C^{-1}_{G,mm'} \times \left(G_{m'} - \sum_{n'} W_{m'n'} F_{n'} \right), \tag{6}$$

where the subscripts denote the matrix elements. We here assume the uncertainties to be uncorrelated and get the usual least-squares figure of merit in which the misfit of each measurement is divided by its uncertainty:

$$\chi^2 = \sum_m \left(\frac{G_m - \sum_n W_{mn} F_n}{\sigma_{G,m}} \right)^2 = \sum_m \left(\frac{G_m}{\sigma_{G,m}} - \sum_n \frac{W_{mn}}{\sigma_{G,m}} F_n \right)^2. \tag{7}$$

In matrix form this becomes

$$\chi^2 = | \hat{G} - \hat{W} F |^2. \tag{8}$$

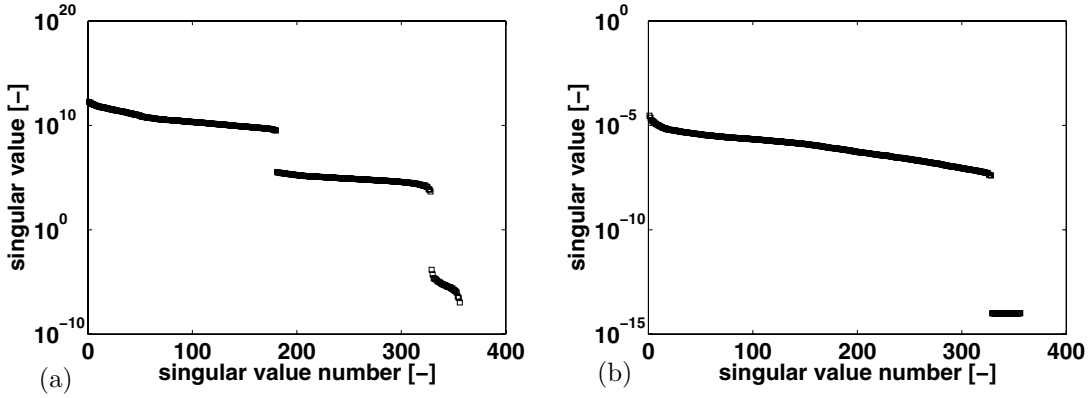

Figure 2. (*a*) Singular values of the transfer matrix W for combined CTS and FIDA measurements (before normalization with the uncertainties). (*b*) Singular values of the transfer matrix $\hat{W}$ for combined CTS and FIDA measurements (after normalization with the uncertainties).

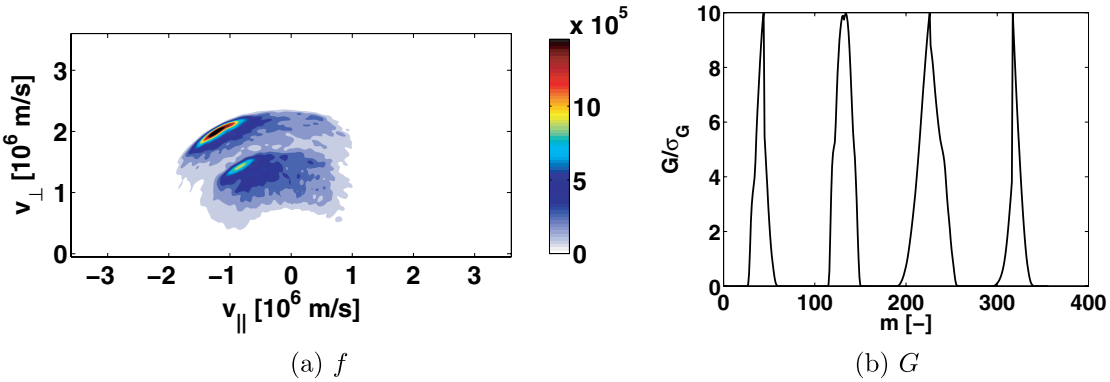

Figure 3. (*a*) 2D velocity distribution function f on a very fine grid (300 × 601). (*b*) Synthetic measurement data in G from two CTS views with $\phi = (33^\circ, 85^\circ)$ (left bumps) and two FIDA views with $\phi = (11^\circ, 64^\circ)$ (right bumps). m is the index of the measurement.

The matrix elements of $\hat{G}$ and $\hat{W}$ are given by

$$\hat{G}_m = G_m/\sigma_{G,m} \tag{9}$$

$$\hat{W}_{mn} = W_{mn}/\sigma_{G,m}, \tag{10}$$

where repeated indices do *not* imply summation. We find a minimum χ^2 figure of merit under minimum two-norm regularization and positivity constraint using the Moore–Penrose pseudoinverse $\hat{W}^+$ [61, 62] computed from the singular value decomposition of $\hat{W}$ [63]. Therefore, the tomographic inversion F^+ is determined from the measurements and their uncertainties by

$$F^+ = \hat{W}^+\hat{G}. \tag{11}$$

F^+ is the least-squares fit to the normalized set of equations

$$\hat{W}F = \hat{G}. \tag{12}$$

In [13] the figure of merit was simply

$$\chi^2 = \mid G - WF \mid^2 \tag{13}$$

which is minimized by

$$F^+ = W^+G \tag{14}$$

as the best-fit solution to equation (5). Equations (5) and (12) are equivalent, but here the figure of merit χ^2 (equation (8)) is different than in [13] (equation (13)). By this normalization of W and G with σ_G here we take the uncertainties of the individual measurements into account. If all uncertainties are equal, the reconstruction prescription in [13] is recovered.

The normalization of the measurements and the weight functions by their respective uncertainties is also essential to improve the conditioning of the transfer matrix. Without this normalization the conditioning of W would usually be poor for combined CTS and FIDA measurements because CTS and FIDA measure different physical quantities, and their weight functions are usually given in different units and have amplitudes that differ by orders of magnitude. The conditioning of $\hat{W}$, in contrast, should usually be good, and this well-conditioned transfer matrix allows the combination of CTS and FIDA measurements. The singular values before and after the normalization by the uncertainties are shown in figure 2. Here we assume the uncertainty in each view to be 10% of the maximum value of the respective view.

4. Joint tomographic inversion from combined CTS and FIDA measurements

First we illustrate the data we use for the inference of F^+. Figure 3(*a*) shows a beam ion velocity distribution function for NBI source S3 (60 keV, 2.5 MW) at ASDEX Upgrade computed with TRANSP/NUBEAM, and figure 3(*b*) shows a set of normalized, synthetic CTS and FIDA measurements of that function. The resolution of the original function, from

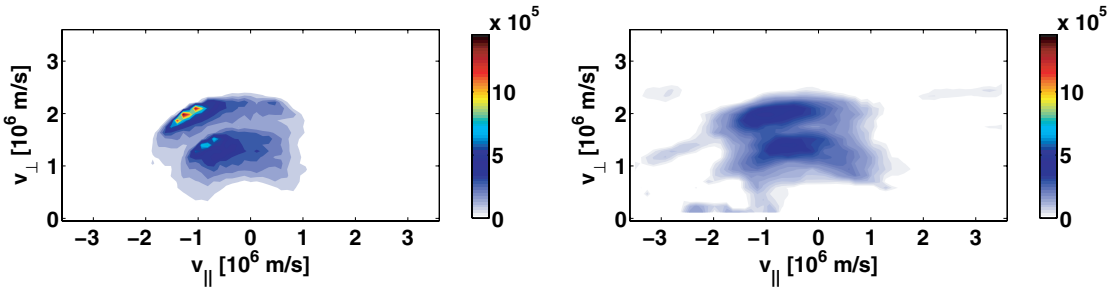

(a) (b) 0%, 200 SV

Figure 4. (*a*) Interpolation of the original function from figure 3(*a*) to the 30 × 61 grid of the tomographic inversion. (*b*) Inversion using 200 singular values. No additional noise has been added to G. The colour scales in (*a*) and (*b*) are identical. Figure 5(*e*) presents the inversion with a different colour scale.

which we take the synthetic measurements, is 300 × 601 grid points. The two bumps to the left in figure 3(*b*) represent CTS measurements taken in two views at $\phi = (33^\circ, 85^\circ)$, and the two bumps to the right represent FIDA measurements at $\phi = (11^\circ, 64^\circ)$ for the two FIDA views. The CTS measurements are distributed in the u-intervals $-5 \times 10^6 < u < -0.7 \times 10^6\,\mathrm{m\,s^{-1}}$ and $0.7 \times 10^6 < u < 5 \times 10^6\,\mathrm{m\,s^{-1}}$ with a resolution of $\Delta u = 0.1 \times 10^6\,\mathrm{m\,s^{-1}}$ that is roughly achievable with the filterbank receivers at ASDEX Upgrade. We do not use CTS measurements in the interval $-0.7 \times 10^6 < u < 0.7 \times 10^6\,\mathrm{m\,s^{-1}}$ because bulk ions make unambiguous detection of fast ions very difficult if not impossible in this interval. The FIDA measurements are evenly distributed in the wavelength intervals 649 nm $< \lambda <$ 654 nm and 659 nm $< \lambda <$ 663 nm. FIDA light cannot be observed in the wavelength interval 654 nm $< \lambda <$ 659 nm due to beam emission and halo neutrals [7], and we likewise exclude this wavelength range in the synthetic measurements. Figure 3(*b*) contains the synthetic normalized measurements that we use for the inference of the tomographic inversions. The abscissa is the measurement index label m that runs from 1 to M, and the ordinate is the corresponding CTS or FIDA measurement normalized by the uncertainty of the measurement (10% of the maxima of each CTS or FIDA view as explained above).

The inversions are calculated on a much coarser grid with 30 × 61 grid points corresponding to velocity-space resolution of typical simulations. The original function has been interpolated to the coarser grid of the inversion in figure 4(*a*) to illustrate an upper limit of the achievable resemblance between the inversion and the original function. If the data are noisy, it is necessary to truncate the SVD and use lower rank approximations to the Moore–Penrose pseudoinverse. Explicit noise will be added in section 5 whereas in this section the noise originates from the different discretizations of the original function (300 × 601) and the inversion (30 × 61). Here the transfer matrix W has a rank of about 320, corresponding to 320 significant singular values (see figure 2(*b*)). In truncated SVD, only the largest singular values are used. Figure 4(*b*) shows a inversion using 200 singular values. The joint inversion from a mix of CTS and FIDA measurements reproduces the overall shape of the underlying function including the location of the peaks at full and half beam injection energy. However, these peaks are broader in the inversion than in the original function, and their amplitudes are approximately 3–4 times smaller.

Figure 5 shows inversions computed with various truncation levels from 40 singular values to 320 singular values. From here on we use different colour scales in the inversions to emphasize the shape of the inferred inversions more clearly. The two peaks at full and half beam injection energies emerge if about 80 singular values are used. The peak amplitudes become larger if more singular values are used, but they never become quite as large as in the original. Using more singular values, however, also tends to increase the jitter in the inversion.

It should be possible to improve the resemblance of the inversions with the original velocity distribution function by adding more CTS or FIDA views or other fast-ion measurements and by increasing the frequency resolution of the measurements [13]. High-frequency resolution CTS measurements on the order of 1 MHz were recently demonstrated which give a few thousand measurements in frequency space per view [64–66].

5. Joint tomographic inversions from noisy measurements

In the following we investigate inversions computed from noisy measurements. Noise makes the smallest singular values useless, and the inversions then have to be inferred using only the largest singular values. The lower the noise level, the more singular values can be used. We add various levels of uncorrelated Gaussian noise to the synthetic measurements and infer inversions at various truncation levels of the SVD.

Figure 6 shows inversions computed for a Gaussian noise level of 2%. The two beam injection peaks again emerge if about 80 singular values are used. About 240 singular values contain useful information at 2% noise. In figure 7 we infer inversions at various noise levels up to 50%. The two peaks at full and half beam injection energy are visible for 100 singular values at noise levels of 4% (figure 7(*a*)). At 10% noise (figure 7(*b*)), the form of the peaks is distorted by the noise, and for larger noise levels such as 20% they completely disappear (figure 7(*c*)) in the jitter. Nevertheless, even at a noise level of 50%, the inversion based on 20 singular values still reveals the coarsest anisotropy features of the original function (figure 7(*d*)).

For a matrix equation of the form $F^+ = \hat{W}^+ \hat{G}$, we can investigate the propagation of errors from the normalized measurements $\hat{G}$ to the inversion F^+. The measurements can contain correlated noise that can be summarized in the $m \times m$

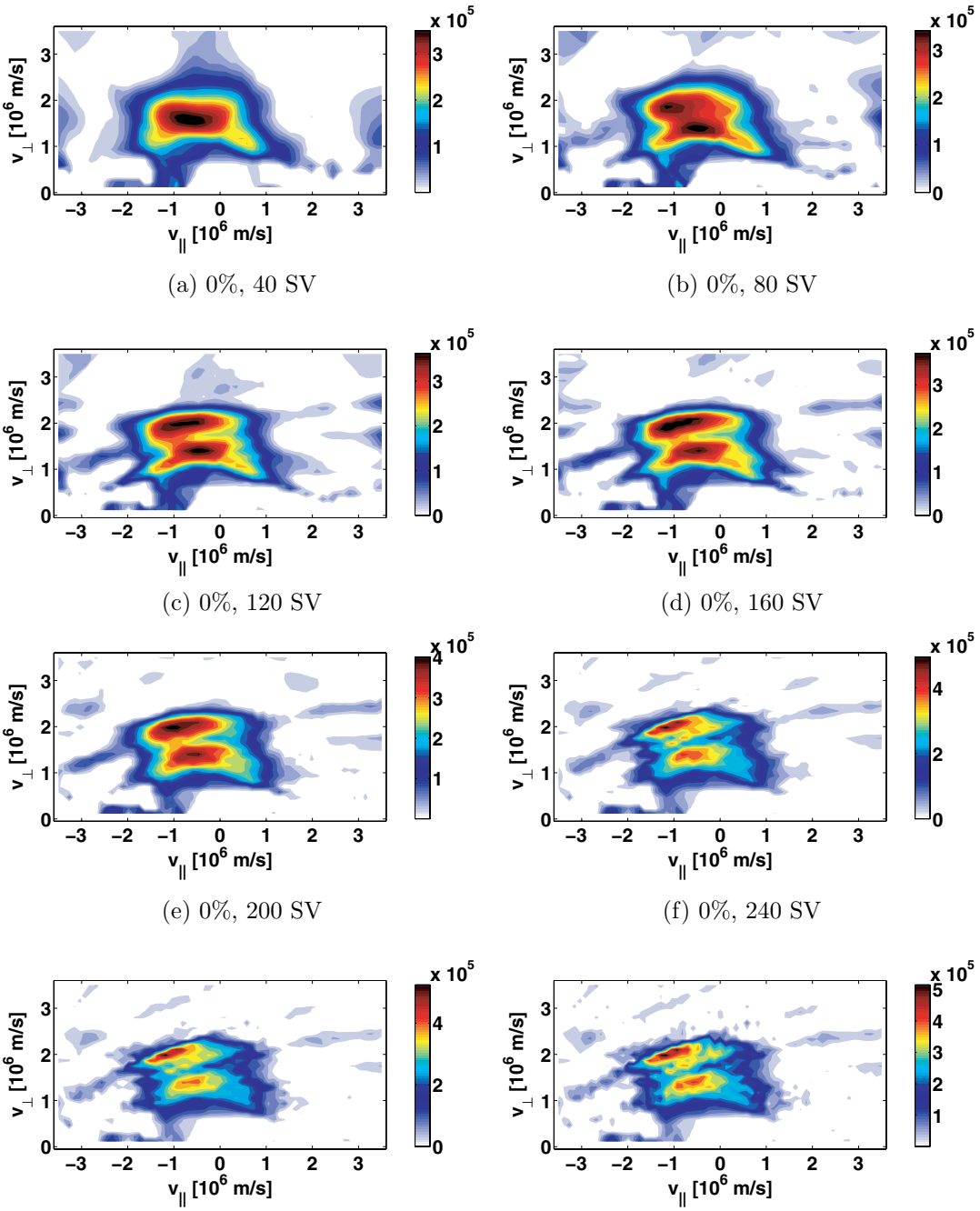

(a) 0%, 40 SV (b) 0%, 80 SV

(c) 0%, 120 SV (d) 0%, 160 SV

(e) 0%, 200 SV (f) 0%, 240 SV

(g) 0%, 280 SV (h) 0%, 320 SV

Figure 5. Tomographic inversions inferred from the synthetic CTS/FIDA four-view data in figure 3(*b*). 40–320 singular values are used in (*a*) to (*h*). No additional noise has been added to G. The colour scales are different from that of the original in figure 4.

covariance matrix $\hat{C}_G$. We then use standard error propagation methods [60] to find the $n \times n$ covariance matrix C_F^+ of F^+:

$$C_F^+ = \hat{W}^+ \hat{C}_G (\hat{W}^+)^T. \tag{15}$$

For uncorrelated noise in the measurements, the diagonal elements $(\sigma_{F,n}^+)^2$ of C_F^+ are given by

$$(\sigma_{F,n}^+)^2 = \sum_m (\hat{W}_{nm}^+)^2 \hat{\sigma}_{G,m}^2. \tag{16}$$

Figure 8 shows standard deviations σ_f^+, which are immediately given by the vectors σ_F^+, using 100 singular values (*a*) and 300 singular values (*b*). Tomographic inferences using only the largest singular values are less sensitive to noise than those using many singular values. For 100 singular values, the values of f are well above the noise level σ_f^+, and hence a tomographic inversion f^+ using 100 singular values is dominated by the measured values g. In contrast, for 300 singular values, the values of f are below the noise level σ_f^+, and hence this inversion f^+ is strongly influenced by noise.

6. The complementary nature of CTS and FIDA measurements

Lastly, we remark that the velocity-space interrogation regions of CTS and FIDA measurements and the relative weightings

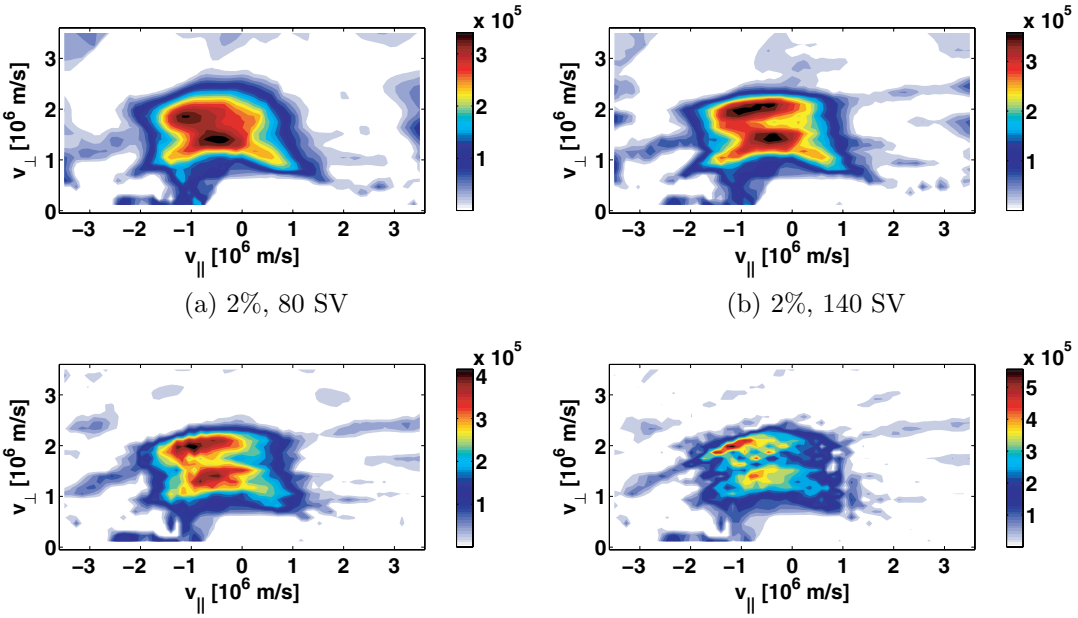

(a) 2%, 80 SV (b) 2%, 140 SV

(c) 2%, 200 SV (d) 2%, 240 SV

Figure 6. Tomographic inversions inferred from the synthetic CTS/FIDA four-view data in figure 3(*b*) with 2% Gaussian noise. 80–240 singular values are used. The colour scales are different from that of the original in figure 4.

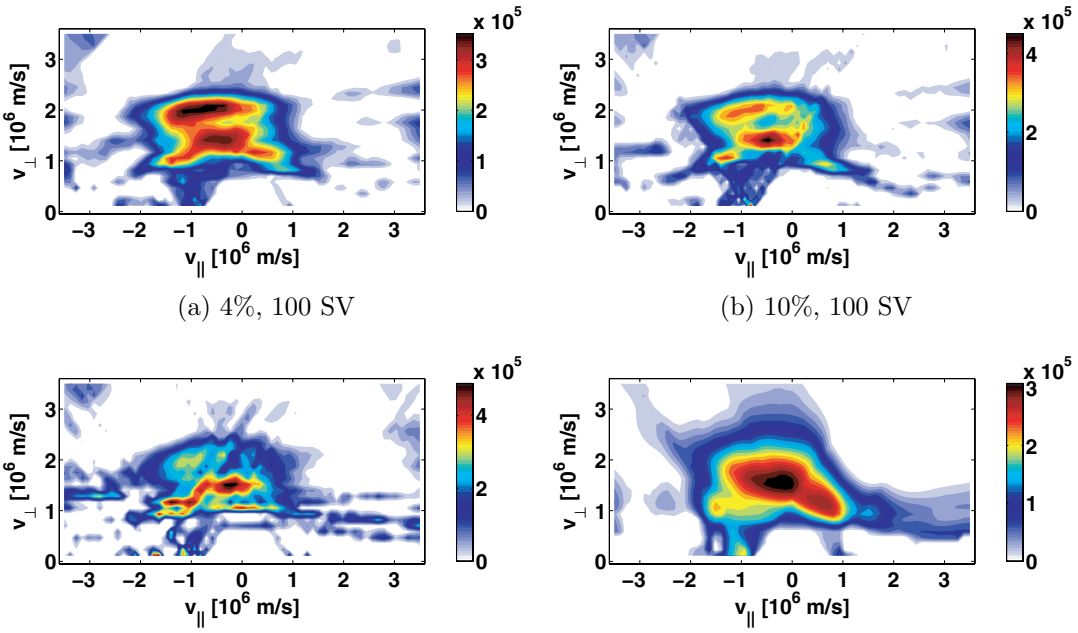

(a) 4%, 100 SV (b) 10%, 100 SV

(c) 20%, 100 SV (d) 50%, 20 SV

Figure 7. Tomographic inversions inferred from the synthetic CTS/FIDA four-view data in figure 3(*b*) with 4–50% Gaussian noise. In (*a*) to (*c*) we use 100 singular values, in (*d*) we use 20 singular values. The colour scales are different from that of the original in figure 4.

within these can in fact never coincide, irrespective of how we choose the scattering geometry. These weightings are described by the weight functions w that relate the 2D velocity-space $(v_\parallel, v_\perp)$ to the 1D CTS or FIDA measurements of a spectrum of radiation. CTS and FIDA measurements g are sensitive to products of their respective weight functions and the ion velocity distribution function f according to equations (1) and (2). The basic shapes of CTS and FIDA velocity-space interrogation regions were illustrated in figure 1. They are given by 1D projections of velocities of gyrating ions determining the frequency shifts of detectable radiation [34]. Despite the identical projection angle in figure 1, the boundaries of the triangular velocity-space interrogation region of FIDA have a smaller slope than those for CTS due to Stark splitting: Stark splitting broadens the FIDA velocity-space interrogation regions compared with those of CTS. The weights are also different due to Stark splitting, the charge-exchange probability, and the probability of a Balmer alpha photon emission. Figure 1 suggests that the observable signals emphasize different velocity-space regions even if the interrogation regions are chosen to be as similar as possible. This makes direct comparisons of CTS and FIDA

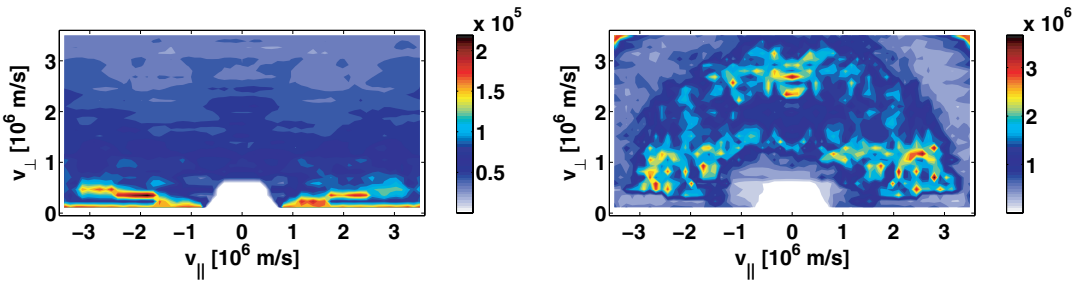

(a) 100 SV (b) 300 SV

Figure 8. Standard deviation σ_f^+ of the inversion obtained from the diagonal elements of the covariance matrix for (*a*) 100 singular values and (*b*) 300 singular values.

measurements difficult as these measurements can never be redundant; they are complementary irrespective of the viewing geometry. But the combination of the measurements in joint inversions turns this intrinsically complementary nature of the measurements into an advantage. One may then speculate how to set the projection angles of the available CTS and FIDA views to obtain the best possible inversion and how many views are really required. It is firstly beneficial to increase the number of views and secondly to select very different projection angles in each view as one would intuitively expect. It is, however, outside the scope of this work to find optimum projection angles or number of views, and we will give comprehensive discussion of these topics elsewhere.

7. Conclusions

We have demonstrated that diagnostic information from CTS and FIDA measurements can be combined in joint velocity-space tomographic inversions that provide the best fit to the measurements under a regularization condition. To enable this combination of diagnostic methods, we have derived a new velocity-space tomography prescription that can use information from any fast-ion diagnostic and that takes uncertainties in the measurements into account. We infer tomographic reconstructions using synthetic measurements with the combined four-view CTS/FIDA system at ASDEX Upgrade. The synthetic measurements are based on a beam ion velocity distribution function simulated with TRANSP/NUBEAM. The overall shape of the distribution function and the location of the maxima at full and half beam injection energy are reproduced well in tomographic inversions, if uncorrelated Gaussian noise in the measurements has a level below 10%. Joint tomography using real fast-ion measurements can combine different diagnostic methods—also other than CTS and FIDA—and can yield an experimentally determined 2D fast-ion velocity distribution function.

Acknowledgments

This work, supported by the European Communities under the contract of Association between Euratom and DTU, was partly carried out within the framework of the European Fusion Development Agreement. The views and opinions expressed herein do not necessarily reflect those of the European Commission.

References

[1] Gruber O. 2007 Overview of ASDEX Upgrade results *Nucl. Fusion* **47** S622–34
[2] Kallenbach A. *et al* 2012 Recent ASDEX Upgrade results and future extension plans *IEEE Trans. Plasma Sci.* **40** 605–13
[3] Stroth U. *et al* 2013 Overview of ASDEX Upgrade results *Proc. 24th Conf. on Fusion Energy (San Diego, 8–13 October 2012)* www-naweb.iaea.org/napc/physics/FEC/FEC2012/html/fec12.htm; *Nucl. Fusion* at press
[4] García-Muñoz M., Martin P., Fahrbach H.-U., Gobbin M., Günter S., Maraschek M., Marrelli L., Zohm H. and the ASDEX Upgrade Team 2007 NTM induced fast ion losses in ASDEX Upgrade *Nucl. Fusion* **47** L10–5
[5] García-Muñoz M. *et al* 2009 MHD induced fast-ion losses on ASDEX Upgrade *Nucl. Fusion* **49** 085014
[6] Garcia-Munoz M. *et al* 2011 Fast-ion transport induced by Alfvén eigenmodes in the ASDEX Upgrade tokamak *Nucl. Fusion* **51** 103013
[7] Geiger B., Garcia-Munoz M., Heidbrink W.W., McDermott R.M., Tardini G., Dux R., Fischer R. and Igochine V. 2011 Fast-ion D-alpha measurements at ASDEX Upgrade *Plasma Phys. Control. Fusion* **53** 065010
[8] Meo F. *et al* 2008 Commissioning activities and first results from the collective Thomson scattering diagnostic on ASDEX Upgrade (invited) *Rev. Sci. Instrum.* **79** 10E501
[9] Salewski M. *et al* 2010 Comparison of fast ion collective Thomson scattering measurements at ASDEX Upgrade with numerical simulations *Nucl. Fusion* **50** 035012
[10] Meo F. *et al* and The Asdex Upgrade Team 2010 First results and analysis of collective Thomson scattering (CTS) fast ion distribution measurements on ASDEX Upgrade *J. Phys.: Conf. Ser.* **227** 012010
[11] Furtula V., Salewski M., Leipold F., Michelsen P.K., Korsholm S.B., Meo F., Moseev D., Nielsen S.K., Stejner M. and Johansen T. 2012 Design and performance of the collective Thomson scattering receiver at ASDEX Upgrade *Rev. Sci. Instrum.* **83** 013507
[12] Furtula V., Leipold F., Salewski M., Michelsen P.K., Korsholm S.B., Meo F., Moseev D., Nielsen S.K., Stejner M. and Johansen T. 2012 Performance measurements of the collective Thomson scattering receiver at ASDEX Upgrade *J. Instrum.* **7** C02039
[13] Salewski M. *et al* 2012 Tomography of fast-ion velocity-space distributions from synthetic CTS and FIDA measurements *Nucl. Fusion* **52** 103008
[14] Giacomelli L., Zimbal A., Tittelmeier K., Schuhmacher H., Tardini G. and Neu R. 2011 The compact neutron spectrometer at ASDEX Upgrade *Rev. Sci. Instrum.* **82** 123504
[15] Tardini G., Zimbal A., Esposito B., Gagnon-Moisan F., Marocco D., Neu R., Schuhmacher H. and the

ASDEX Upgrade Team 2012 First neutron spectrometry measurements in the ASDEX Upgrade tokamak *J. Instrum.* **7** C03004
[16] Kurki-Suonio T., Hynönen V., Suttrop W., Fahrbach H.-U., Stober J. and the ASDEX Upgrade Team 2006 Edge fast ion distribution benchmarking ASCOT against experimental NPA data on ASDEX Upgrade *Europhys. Conf. Abstracts* vol 30I p P2.145
[17] Äkäslompolo S., Hirvijoki E., Kurki-Suonio T. and the ASDEX Upgrade Team 2010 Implementing beam-beam CX-reactions in the ASCOT-code and prediction of active NPA measurement *Europhys. Conf. Abstracts* vol 34A p P5.113
[18] Nocente M. *et al* and the ASDEX Upgrade Team 2012 Gamma-ray spectroscopy measurements of confined fast ions on ASDEX upgrade *Nucl. Fusion* **52** 094021
[19] Moseev D. *et al* 2011 Comparison of measured and simulated fast ion velocity distributions in the TEXTOR tokamak *Plasma Phys. Control. Fusion* **53** 105004
[20] Heidbrink W.W. 2010 Fast-ion Dα measurements of the fast-ion distribution (invited) *Rev. Sci. Instrum.* **81** 10D727
[21] Kak A.C. and Slaney M. 1988 *Principles of Computerized Tomographic Imaging* (New York: IEEE Press)
[22] Herman G.T. 2009 *Fundamentals of Computerized Tomography* 2nd edn (Berlin: Springer)
[23] Ertl K., von der Linden W., Dose V. and Weller A. 1996 Maximum entropy based reconstruction of soft x-ray emissivity profiles in W7-AS *Nucl. Fusion* **36** 1477–88
[24] Anton M., Weisen H., Dutch M.J., von der Linden W., Buhlmann F., Chavan R., Marletaz B., Marmillod P. and Paris P. 1996 X-ray tomography on the TCV tokamak *Plasma Phys. Control. Fusion* **38** 1849–78
[25] Ingesson L.C., Alper B., Chen H., Edwards A.W., Fehmers G.C., Fuchs J.C., Giannella R., Gill R.D., Lauro-Taroni L. and Romanelli M. 1998 Soft x ray tomography during ELMs and impurity injection in JET *Nucl. Fusion* **38** 1675–94
[26] Nagayama Y., Taylor G., Yamada M., Fredrickson E.D., Janos A.C. and McGuire K.M. 1996 ECE image reconstruction of partial sawtooth crashes in ohmic plasmas *Nucl. Fusion* **36** 521–6
[27] Howard J. 1996 Vector tomography applications in plasma diagnostics *Plasma Phys. Control. Fusion* **38** 489–503
[28] Konoshima S., Leonard A.W., Ishijima T., Shimizu K., Kamata I., Meyer W.H., Sakurai S., Kubo H., Hosogane N. and Tamai H. 2001 Tomographic reconstruction of bolometry for JT-60U diverted tokamak characterization *Plasma Phys. Control. Fusion* **43** 959–83
[29] Peterson B.J., Kostrioukov A.Yu., Ashikawa N., Liu Y., Yuhong Xu., Osakabe M., Watanabe K.Y., Shimozuma T., Sudo S. and the LHD Experiment Group 2003 Bolometer diagnostics for one- and two-dimensional measurements of radiated power on the Large Helical Device *Plasma Phys. Control. Fusion* **45** 1167–82
[30] Furno I., Weisen H., Carey C., Angioni C., Behn R., Fable E., Zabolotsky A., the TCV Team, and JET-EFDA Contributors 2005 A new method for the inversion of interferometry data using basis functions derived from singular value decomposition of local measurements in tokamak plasmas *Plasma Phys. Control. Fusion* **47** 49–69
[31] Bonheure G., Popovichev S., Bertalot L., Murari A., Conroy S., Mlynar J., Voitsekhovitch I. and JET-EFDA Contributors 2006 Neutron profiles and fuel ratio n T/n D measurements in JET ELMy H-mode plasmas with tritium puff *Nucl. Fusion* **46** 725–40
[32] Svensson J. and Werner A. 2008 Current tomography for axisymmetric plasmas *Plasma Phys. Control. Fusion* **50** 085002
[33] Egedal J. and Bindslev H. 2004 Reconstruction of gyrotropic phase-space distributions from one-dimensional projections *Phys. Plasmas* **11** 2191
[34] Salewski M. *et al* 2011 On velocity space interrogation regions of fast-ion collective Thomson scattering at ITER *Nucl. Fusion* **51** 083014
[35] Nielsen S.K. *et al* 2010 Fast-ion redistribution due to sawtooth crash in the TEXTOR tokamak measured by collective Thomson scattering *Plasma Phys. Control. Fusion* **52** 092001
[36] Nielsen S.K. *et al* 2011 Dynamics of fast ions during sawtooth oscillations in the TEXTOR tokamak measured by collective Thomson scattering *Nucl. Fusion* **51** 063014
[37] Pace D.C. *et al* 2011 Transport of energetic ions due to sawteeth, Alfvén eigenmodes and microturbulence *Nucl. Fusion* **51** 043012
[38] Muscatello C.M., Heidbrink W.W., Kolesnichenko Ya.I., Lutsenko V.V., Van Zeeland M.A. and Yakovenko Yu.V. 2012 Velocity-space studies of fast-ion transport at a sawtooth crash in neutral-beam heated plasmas *Plasma Phys. Control. Fusion* **54** 025006
[39] Heidbrink W.W. and Sadler G.J. 1994 The behaviour of fast ions in tokamak experiments *Nucl. Fusion* **34** 535–615
[40] Zweben S.J., Budny R.V., Darrow D.S., Medley S.S., Nazikian R., Stratton B.C., Synakowski E.J. and Taylor G. for the TFTR Group 2000 Alpha particle physics experiments in the Tokamak Fusion Test Reactor *Nucl. Fusion* **40** 91–149
[41] Nabais F., Borba D., Garcia-Muñoz M., Johnson T., Kiptily V.G., Reich M., Nave M.F.F., Pinches S.D. and Sharapov S.E. 2010 Impact of strongly driven fishbones and Alfvén eigenmodes on fast ion losses *Nucl. Fusion* **50** 115006
[42] Van Zeeland M.A. *et al* 2011 Measurements and modeling of Alfvén eigenmode induced fast ion transport and loss in DIII-D and ASDEX Upgrade 2011 *Phys. Plasmas* **18** 056114
[43] Pace D.C., Fisher R.K., García-Muñoz M., Heidbrink W.W. and Van Zeeland M.A. 2011 Convective beam ion losses due to Alfvén eigenmodes in DIII-D reversed-shear plasmas *Plasma Phys. Control. Fusion* **53** 062001
[44] Günter S. *et al* and the ASDEX Upgrade Team 2007 Interaction of energetic particles with large and small scale instabilities *Nucl. Fusion* **47** 920–8
[45] Dannert T., Günter S., Hauff T., Jenko F., Lapillonne X. and Lauber P. 2008 Turbulent transport of beam ions *Phys. Plasmas* **15** 062508
[46] Hauff T. and Jenko F. 2008 Mechanisms and scalings of energetic ion transport via tokamak microturbulence *Phys. Plasmas* **15** 112307
[47] Hauff T., Pueschel M., Dannert T. and Jenko F. 2009 Electrostatic and magnetic transport of energetic ions in turbulent plasmas *Phys. Rev. Lett.* **102** 075004
[48] Graves J.P., Chapman I.T., Coda S., Lennholm M., Albergante M. and Jucker M. 2012 Control of magnetohydrodynamic stability by phase space engineering of energetic ions in tokamak plasmas *Nature Commun.* **3** 624
[49] Kubo S. *et al* 2010 Collective Thomson scattering of a high power electron cyclotron resonance heating beam in LHD (invited) *Rev. Sci. Instrum.* **81** 10D535
[50] Ito T., Osakabe M., Ida K., Yoshinuma M., Kobayashi M., Murakami S., Goto M., Takeiri Y., Reiter D. and Okamura S. 2012 Effect of halo neutrals on fast-ion charge exchange spectroscopy measurements in LHD *Plasma Fusion Res.* **5** S2099
[51] Kappatou A., Delabie E., Jaspers R.J.E. and von Hellermann M.G. 2012 Feasibility of non-thermal helium measurements with charge exchange spectroscopy on ITER *Nucl. Fusion* **52** 043007

[52] Salewski M., Meo F., Bindslev H., Furtula V., Korsholm S.B., Lauritzen B., Leipold F., Michelsen P.K., Nielsen S.K. and Nonbø l E. 2008 Investigation of first mirror heating for the collective Thomson scattering diagnostic in ITER *Rev. Sci. Instrum.* **79** 10E729

[53] Salewski M. *et al* 2009 Comparison of collective Thomson scattering signals due to fast ions in ITER scenarios with fusion and auxiliary heating *Plasma Phys. Control. Fusion* **51** 035006

[54] Salewski M., Eriksson L.-G., Bindslev H., Korsholm S.B., Leipold F., Meo F., Michelsen P.K. and Nielsen S.K. 2009 Impact of ICRH on the measurement of fusion alphas by collective Thomson scattering in ITER *Nucl. Fusion* **49** 025006

[55] Leipold F., Furtula V., Salewski M., Bindslev H., Korsholm S.B., Meo F., Michelsen P.K., Moseev D., Nielsen S.K. and Stejner M. 2009 Antenna design for fast ion collective Thomson scattering diagnostic for the international thermonuclear experimental reactor *Rev. Sci. Instrum.* **80** 093501

[56] Heidbrink W.W., Luo Y., Burrell K.H., Harvey R.W., Pinsker R.I. and Ruskov E. 2007 Measurements of fast-ion acceleration at cyclotron harmonics using Balmer-alpha spectroscopy *Plasma Phys. Control. Fusion* **49** 1457–75

[57] Heidbrink W.W. *et al* 2008 Central flattening of the fast-ion profile in reversed-shear DIII-D discharges *Nucl. Fusion* **48** 084001

[58] Muscatello C.M., Heidbrink W.W., Taussig D. and Burrell K.H. 2010 Extended fast-ion D-alpha diagnostic on DIII-D *Rev. Sci. Instrum.* **81** 10D316

[59] Bortolon A., Heidbrink W.W. and Podestà M. 2010 A tangentially viewing fast ion D-alpha diagnostic for NSTX *Rev. Sci. Instrum.* **81** 10D728

[60] Barlow R.J. 1989 *Statistics* (New York: Wiley)

[61] Moore E.H. 1920 14th Western Meeting of the American Mathematical Society *Bull. Am. Math. Soc.* **26** 385–96

[62] Penrose R. 1955 A generalized inverse for matrices *Math. Proc. Cambridge Phil. Soc.* **51** 406–13

[63] Strang G. 1988 *Linear Algebra and its Applications* (Orlando, FL: Harcourth Brace Jovanovich)

[64] Stejner M. *et al* 2010 Collective Thomson scattering measurements with high frequency resolution at TEXTOR *Rev. Sci. Instrum.* **81** 10D515

[65] Korsholm S.B. *et al* 2011 Measurements of intrinsic ion Bernstein waves in a tokamak by collective thomson scattering *Phys. Rev. Lett.* **106** 165004

[66] Stejner M. *et al* 2012 Measurements of plasma composition in the TEXTOR tokamak by collective Thomson scattering *Plasma Phys. Control. Fusion* **54** 015008